Atomic-scale surface restructuring of copper electrodes under CO_2 electroreduction conditions

Reihaneh Amirbeigiarab[1], Jing Tian[1], Antonia Herzog [2], Canrong Qiu[1,3], Arno Bergmann [2], Beatriz Roldan Cuenya [2] & Olaf M. Magnussen [1]✉

Potentiodynamic methods that induce structural changes in Cu catalysts for the electrochemical reduction of CO_2 (CO_2RR) have been identified as a promising strategy for steering the catalyst selectivity towards the generation of multi-carbon products. In current approaches, active species are created via a sequential Cu oxidation–reduction process. Here we show by in situ scanning tunnelling microscopy, surface X-ray diffraction and Raman spectroscopy measurements that low-coordinated Cu surface species form spontaneously near the onset of CO_2 electrocatalytic reduction. This process starts by CO-induced Cu nanocluster formation in the initial stages of the reaction, leading to irreversible surface restructuring that persists over a wide potential range. On subsequent potential increase, the nanoclusters disperse into Cu adatoms, which stabilize reaction intermediates on the surface. The observed self-induced formation of undercoordinated sites on the CO_2-converting Cu catalyst surface can account for its reactivity and may be exploited to (re)generate active CO_2RR sites by potentiodynamic protocols.

The electrochemical reduction of carbon dioxide (CO_2RR) is a subject of great economic and social relevance as it represents a promising solution for the storage of renewable energy in the form of valuable chemical compounds and fuels[1,2]. The reactivity and selectivity of the CO_2RR depend on the catalyst material as well as on the surface and interfacial structure/composition and the nanoscale morphology of the catalyst[3]. Copper and copper alloys have attracted particular attention because of their unique ability to reduce carbon dioxide to multi-carbon products[4–6]. However, the energy efficiency and selectivity of the CO_2RR on Cu are still far from those required for large-scale industrial applications. Thus, optimization of both the catalyst and the reaction conditions is urgently needed. For a knowledge-based catalyst design and a fundamental understanding of the reaction pathways, the role of intermediates and the impact of each parameter, it is essential to clarify the nanoscale morphological properties of copper catalysts, in particular under the relevant reaction conditions.

Recently, the control of the reactivity and selectivity of the CO_2RR catalyst through potentiodynamic operation conditions has become a topic of great interest[7–9]. It has been shown that pulsed operation between CO_2RR and Cu oxidation regimes can create active states on the catalyst that allow the reaction to be steered towards desirable products, including valuable multi-carbon compounds. In practice, this mode of operation requires periodic reversing of the electrode polarity from cathodic to anodic conditions, which may not be trivial for large-scale electrolysers. Whether similar gains in selectivity can be gained by potential pulses that are restricted to the cathodic regime is not clear at present.

From a fundamental point of view, the success of potentiodynamic operation modes is based on the highly dynamic behaviour of Cu electrode surfaces. Copper shows high surface mobility at room temperature and is known to undergo surface restructuring under different conditions[10]. Under hydrogen evolution conditions,

[1]Institute of Experimental and Applied Physics, Kiel University, Kiel, Germany. [2]Department of Interface Science, Fritz-Haber Institute of the Max-Planck Society, Berlin, Germany. [3]Present address: Deutsches Elektronen-Synchrotron (DESY), Hamburg, Germany. ✉e-mail: magnussen@physik.uni-kiel.de

hydrogen-induced surface reconstruction of Cu(100) and Cu(111) in acidic media at pH < 3 was observed by in situ scanning tunnelling microscopy (STM)[11,12], and the resulting structure could be explained by ab initio calculations[13]. Auer et al. showed that Cu(111) starts to reconstruct in alkaline media at the potential of zero free charge and undergoes full reconstruction at higher potentials[14]. Moreover, substantial restructuring of polycrystalline Cu, resulting in a preferential exposure of (100) facets, was observed by Kim and co-workers[15,16]. Eren et al. studied the surface morphology of Cu by STM and X-ray photoelectron spectroscopy in the presence of CO gas at a pressure of 0.1–100 torr (refs. [17,18]). In the case of Cu(111), triangular- and hexagonal-shaped nanoclusters with diameters of around 0.5 and 1.5 nm, respectively, were observed. Cu(100) started to break up already at a CO pressure of 0.25 mbar to square-shaped nanoclusters consisting of five Cu atoms stabilized by four CO molecules. At ≥20 mbar, the clusters had changed to three-atom-wide one-dimensional nanoclusters oriented along the [001] direction. More recently, Auer et al. revealed a similar dynamic restructuring of Cu(111) in CO-saturated alkaline electrolyte at 0.32 V versus the reversible hydrogen electrode (RHE), where CO electro-oxidation occurs[19]. They reported that cluster formation in the presence of CO is largely reversible and showed by first-principles microkinetic modelling that the formed low-coordinated Cu surface species play a vital role in the CO oxidation process. All these studies indicated a high tendency of the Cu surface to undergo dynamic restructuring on the nanoscale, albeit under different conditions from those found during CO_2 electroreduction.

Studies of Cu electrodes under CO_2RR conditions, mostly in CO_2-saturated bicarbonate solutions at pH ≈ 7, so far have found only larger-scale changes in surface morphology. Lee et al. verified by grazing incidence X-ray diffraction that polycrystalline Cu reconstructs to Cu(100) in CO_2-saturated bicarbonate and showed that the Cu(100) surface fraction increases as a function of the applied potential[20]. Phan et al. revealed the restructuring of polycrystalline copper to Cu nanocuboids under CO_2RR conditions, with the cuboid size being determined by the polarization potential and time[21]. In situ atomic force microscopy (AFM) investigations by Simon et al. demonstrated the roughening of the Cu(100) surface through oxidation by immersion in CO_2-saturated bicarbonate electrolyte at the open circle potential[22]. After Cu oxide reduction, round multilayer Cu islands with atomically flat terraces emerged that transformed into square islands with [110]-oriented steps and an increased number of step sites on decreasing the potential to the CO_2RR range. The same group also observed significant morphology changes in differently prepared Cu(111) and Cu(100) catalysts under CO_2RR conditions in this electrolyte by ex situ AFM in air[23]. We note that these previous studies employed experimental conditions in which initial oxidation of the Cu sample could not be avoided and thus they did not start with an atomically smooth Cu(100) surface. Indirect evidence for surface restructuring was also found in in situ vibrational spectroscopy studies of CO on Cu electrodes[24–26]. In particular, on the basis of their observations, Gunathunge et al. proposed for CO_2RR in KHCO₃ a highly reversible formation of Cu clusters at high coverage of CO intermediates starting at around −0.6 V versus RHE[25]. Furthermore, Cu restructuring was also proposed in studies of Cu nanoparticle agglomeration during the CO_2RR[27,28].

Here we show that atomic-scale dynamic restructuring of copper electrodes also occurs during CO_2RR in neutral carbonate electrolyte. We present high-resolution in situ STM, in situ surface X-ray diffraction (SXRD), and in situ surface-enhanced Raman spectroscopy (SERS) studies of Cu(100) electrodes in CO_2-saturated 0.1 M KHCO₃ that provide direct evidence for CO-promoted surface restructuring, with Cu nanocluster formation in the pre-CO_2RR potential range. Furthermore, we demonstrate that this restructuring causes the irreversible formation of low-coordinated Cu species and a disruption of the structure of the molecular adlayer on the electrode surface.

Results

In situ STM studies of nanoscale surface restructuring

STM studies of Cu(100) electrodes in CO_2-saturated 0.1 M KHCO₃, prepared by a procedure that rigorously avoids Cu oxidation (see Methods for details), revealed a morphology with atomically flat terraces, separated by monoatomic steps, in the potential range above about −0.2 V versus RHE (used as a reference potential throughout this work). On decreasing the potential stepwise, characteristic changes in the surface structure were observed. As illustrated in Fig. 1a, nanosized clusters started to appear at a potential of −0.22 V. On further decreasing the potential to −0.27 V, the cluster density on the terraces increased significantly (Fig. 1b,c). As shown in Fig. 1d, the clusters slowly disappeared when the potential was changed back to −0.12 V. Applying higher potentials of up to 0.13 V led to a completely cluster-free surface in a few minutes (Supplementary Fig. 1), indicating that cluster formation is fully reversible. STM experiments in which the potential was changed to values as low as −0.5 V, that is, in the potential regime where CO_2RR starts, confirmed the behaviour illustrated in Fig. 1 and verified the presence of clusters at these negative potentials, although the STM tip became less stable under these conditions (Supplementary Fig. 2). Also, the clusters formed at these low potentials again completely disappeared after increasing the potential back to positive values.

Based on previous results for closely related systems[17–19], we attribute the observed clusters to CO-promoted Cu nanocluster and adatom formation on the surface. Quantitative analysis of the structural properties of the clusters (Supplementary Fig. 3) showed that the majority of the clusters have diameters of ≤1.5 nm and apparent heights corresponding to a Cu monolayer. However, a small fraction of larger clusters with diameters of up to 5 nm and heights of ≤0.4 nm were also observed. These values are similar to those observed for CO-induced clusters formed on Cu(111) during alkaline CO electro-oxidation and CO adsorption from the gas phase, indicating a common origin despite the very different environment[17,19]. The nanoclusters can be observed close to existing Cu steps and thus will also be formed on Cu surfaces that have been roughened by oxidation on exposure to air and/or electrolyte without potential control, under which conditions the Cu terraces are much narrower (Supplementary Fig. 4). Indeed, small clusters are discernible in some of the in situ AFM images of pre-oxidized Cu(100) presented by Simon et al.[22]. The observed restructuring is therefore also relevant for more realistic complex Cu catalysts.

Interestingly, the cluster formation process caused no noticeable changes in the steps on the Cu surface (Supplementary Figs. 1, 2 and 5), indicating that the atoms in the clusters may not necessarily originate from the edges of the Cu steps. We attribute this behaviour to the presence of (bi)carbonate and other species, which are adsorbed over a very wide potential range on Cu electrodes in carbonate solution (see below), as has also been found in density functional theory (DFT) studies[29,30]. These species most likely block the surface diffusion of Cu adatoms at this moderate overpotential and may also hinder the detachment of Cu atoms from step edges. A similar blocking of step sites by adsorbates has been reported in related systems[31]. If the steps are not the source of the Cu atoms in the clusters, these atoms have to come from the Cu terraces, which implies the formation of vacancies in the Cu surface layer. Evidence for the latter is indeed found in the STM images, which show the emergence of shallow depressions on the terraces simultaneously with cluster formation (example marked by the white arrow in Fig. 1c). The apparent height of these depressions is around 0.03–0.1 nm, clearly less than that expected for monoatomically deep holes in the Cu surface layer. On increasing the potential, the depressions remained on the surface, even after complete dissolution of the cluster, albeit undergoing slow changes in shape. The presence of these depressions at potentials above 0 V excludes the possibility that they are induced by hydrogen, as reported for Cu(100) at pH < 3 in the potential region of the hydrogen evolution reaction[11]. According to a rough estimation by grain analysis methods (similar to those used in
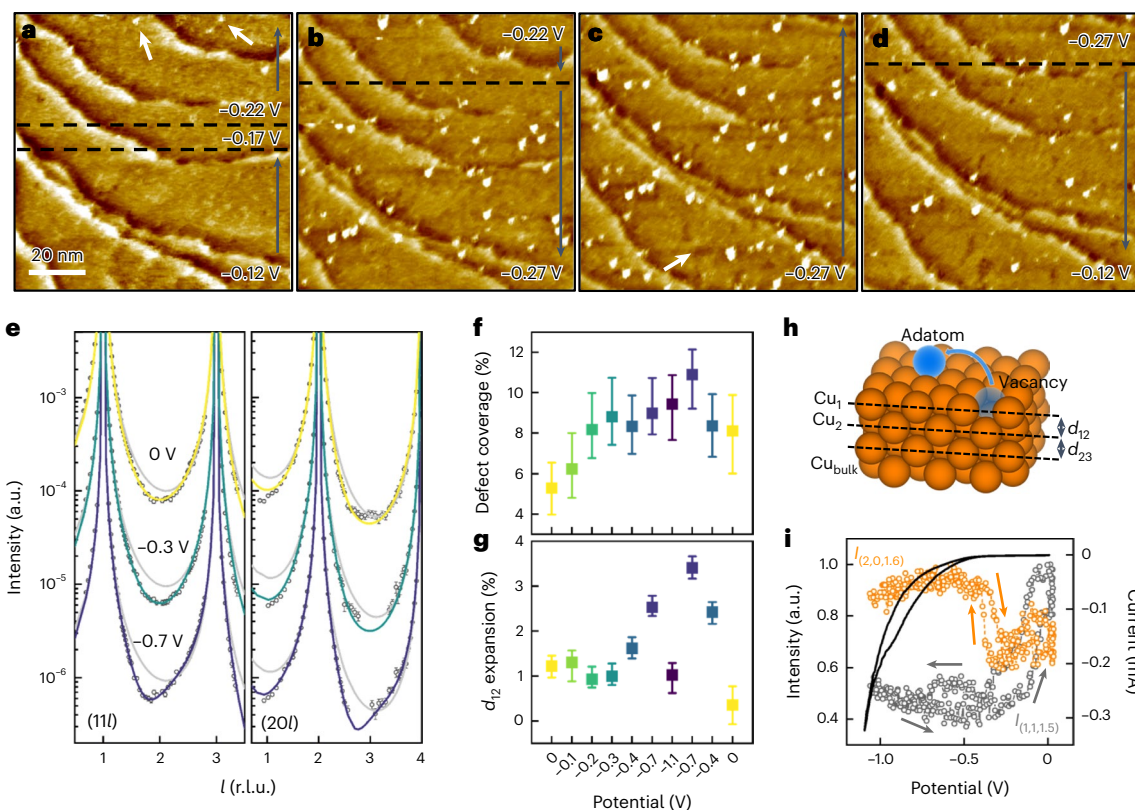
Fig. 1 | Nanoscale surface restructuring of Cu(100) in 0.1 M KHCO₃.
a–**d**, Sequence of in situ STM images recorded during stepwise potential changes from −0.12 to −0.17 and then to −0.22 V (**a**), further decrease to −0.27 V (**b**), where the potential is kept in the subsequent image (**c**), showing nanocluster formation (examples marked by white arrows), and final change back to −0.12 V (**d**), showing the slow disappearance of the clusters. Grey arrows indicate scan direction; regions of constant potential are separated by dashed lines. Images were recorded at intervals of 84 s. **e**, In situ SXRD measurements of the experimentally obtained CTRs (11*l*) and (20*l*) (circles) at 0, −0.3 and −0.7 V (given vs reciprocal lattice units, r.l.u.) and the corresponding best fits (solid coloured lines) using the simple structural model depicted in **h**. Each set of data is offset by a factor of ten. The grey lines show the data for ideal CTRs of a perfectly truncated defect-free crystal. The full CTR datasets are provided in Supplementary Fig. 10.

f,**g**, Coverage of surface defects comprising adatom–vacancy pairs (**f**) and vertical expansion of the d_{12} spacing between the top two Cu layers (**g**) as a function of the applied potential, obtained from the CTR fits. The errors in **f** and **g** correspond to the minima and maxima of all intermediate fits from all fit generations (1,000 generations and 100 populations of each generation) that deviate ≤5% from the optimal figure of merit. **h**, Cu(100) surface model used for fitting the CTR data. The model assumes the presence of surface defects produced by moving atoms from the Cu surface layer (Cu₁) to a lattice position on top of the surface (adatom–vacancy pairs), as well as relaxations in the spacings d_{12} and d_{23} between surface and second layer (Cu₂) and between second layer and the following layer (Cu_bulk) with bulk properties. **i**, Potential-dependent scattered intensity at the reciprocal space positions (2, 0, 1.6) and (1, 1, 1.5) during cyclic voltammograms (example shown as black line) at a scan rate of 5 mV s⁻¹.

Supplementary Fig. 3), the depressions (after cluster dissolution) have, within the precision of the measurement of these nanoscale objects, a similar or somewhat higher coverage (6%) than the clusters (4%). As will be shown in more detail below, the depressions on the terraces most likely result from vacancies in the Cu surface layer created by the restructuring process.

In situ SXRD studies under CO₂RR conditions
The potential range in which CO₂RR occurs could not be studied fully by in situ STM because the ongoing gas evolution destabilizes the STM imaging process. We therefore performed additional in situ SXRD investigations of this system. We first recorded full sets of crystal truncation rods (CTRs) at different potentials. In these experiments, the potential was decreased stepwise from the double layer (0 V) to the CO₂RR (−1.1 V) regime and then increased stepwise back to 0 V. A detailed overview of the experimental procedures, the data analysis and the models used to describe the results are provided in Supplementary Note 1, Supplementary Figs. 9–11 and Supplementary Tables 1–3.

Selected CTRs were measured at 0, −0.3 and −0.7 V during the potential decrease (Fig. 1e and Supplementary Fig. 10 for the full dataset). For the freshly prepared Cu electrode before CO₂ reduction (0 V),

the measured CTR data were only slightly lower than those expected for a perfectly terminated Cu(100) surface. However, after decreasing the potential to −0.3 V, the CTR intensity between the Bragg peaks was clearly lower than that observed at 0 V, indicating a structural change at the surface. In the potential range of the CO₂RR (−0.7 V), further changes in the CTRs, especially the (20*l*) rod, were observed. In particular, the CTRs became asymmetric, with the intensity minimum shifting to smaller *l* values. As these non-specular CTRs are sensitive to surface structural changes that are commensurate with the in-plane substrate lattice, they qualitatively indicate an increase in the roughness and vertical lattice spacings at the electrode surface.

For a quantitative analysis of the potential-dependent changes, the CTR data were fitted by the model illustrated in Fig. 1h. In this model, the roughness was assumed to result from lattice defects in which Cu atoms in the surface layer moved to lattice positions on top of the surface, corresponding to Cu adatoms or atoms in clusters. In addition, vertical expansion of the two top Cu layer spacings (d_{12} and d_{23}) was included. The inclusion of more weakly scattering adsorbate species on the surface (for example, CO, CO₃ and H₂O) was also tested, but did not have a major influence on the results.
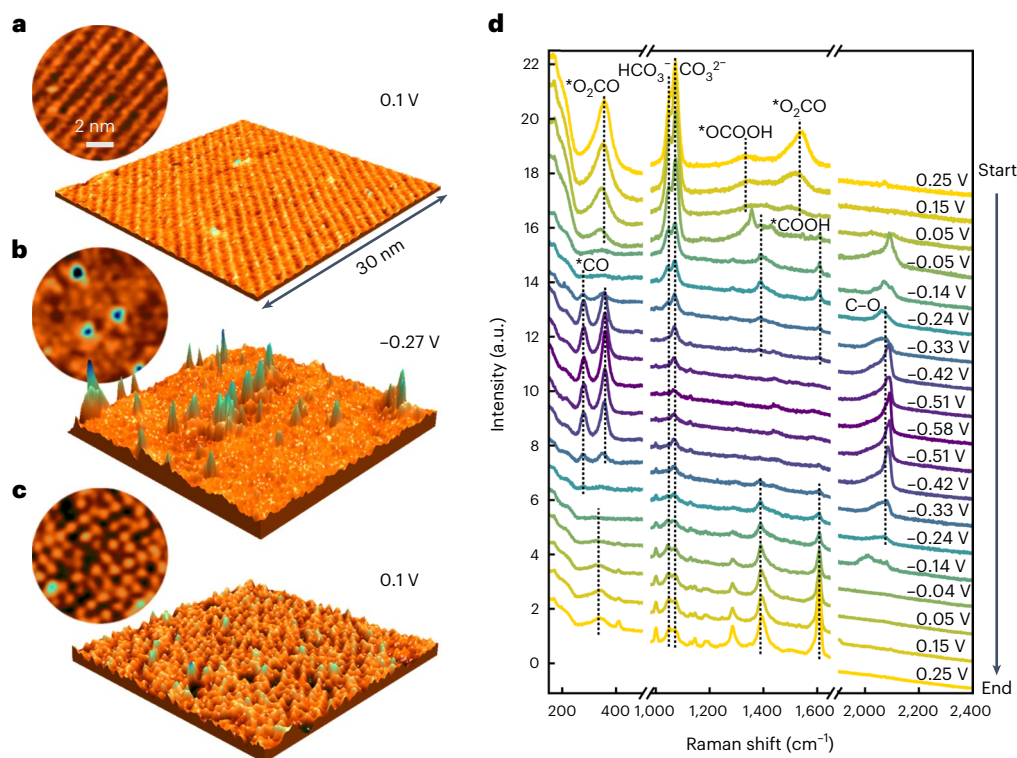
Fig. 2 | Potential-dependent molecular-scale Cu(100) surface structure in CO_2-saturated 0.1 M $KHCO_3$. a–c, Three-dimensional and top-view (circular inset) in situ STM images of the freshly prepared surface at 0.1 V (**a**), −0.27 V (**b**) and after increasing the potential back to 0.1 V (**c**), showing that cluster formation induces irreversible changes in the structure of the molecular adlayer on the surface. **d**, In situ SERS spectra of Cu(100) recorded during stepwise decrease of the potential from 0.25 to −0.58 V and subsequent increase back to 0.25 V (* denotes molecules adsorbed on the Cu surface). The replacement of the initially adsorbed (bi)carbonate by carboxy species and their subsequent replacement by adsorbed CO correlates well with the structural changes observed by in situ STM and SXRD.

The surface density of lattice defects obtained from an analysis of the full sequence of measured CTRs (Fig. 1f) clearly increased at potentials of ≤−0.2 V, in good agreement with the onset of cluster formation in the STM studies. Also, the change in the surface coverage of these defects of ~4% is close to that found by STM. Between −0.2 and −1.1 V, the surface defect density remained constant within the precision of the SXRD measurements, indicating that clusters are present on the surface under CO_2RR conditions and do not further increase in number after their initial formation. This does not exclude other changes in the surface morphology, for example, the step faceting observed by Simon et al.[22], to which the SXRD measurements are insensitive. Interestingly, the density of the lattice defects determined from the CTRs decreased only slightly after increasing the potential back to 0 V, when the Cu clusters disappear according to the STM experiments. This indicates that the Cu atoms in the clusters remain as adatoms on the surface, which will be discussed further below.

The vertical expansion of the topmost atomic Cu layer (Fig. 1g) exhibited a distinctly different potential dependence, indicating that this effect is not directly related to the cluster formation process. Specifically, the expansion remained at a constant value of 1% in the double layer potential range and only started to increase at potentials of ≤−0.4 V, up to a value of 2.5% at −0.7 V. However, it dropped back to 1% at the most negative potential of −1.1 V. This behaviour was observed to be reversible on gradually increasing the potential again, where the potential increased again (to 3.4%) and then decreased. We attribute the potential-dependent expansion to changes in the adsorbate layer on the Cu surface. This is in accordance with in situ SERS and surface-enhanced infrared absorption spectroscopy studies in carbonate electrolyte (see also below), which shows that (bi)carbonate is gradually replaced by CO and other CO_2RR reaction intermediates at potentials of ≤−0.5 V[24–26,32]. However, the bands of these intermediates decreased again below −1 V, concomitant with a decrease in the Faradaic efficiency for C_2 products, indicating that they are rapidly consumed in the catalytic reaction[6,32].

The CTR studies required a recording time of ~1 h per dataset and thus they represent the steady-state behaviour of the system. To investigate the potential-dependent changes under more dynamic conditions, we also measured the X-ray intensity at selected reciprocal space positions along the CTRs during cyclic voltammetry experiments (Fig. 1i), which are on a similar timescale as the STM measurements. These experiments were performed after the CTR measurements on the same sample. At the reciprocal space position of (1, 1, 1.5), the intensity decreased smoothly between −0.1 and −0.3 V, resembling the changes in defect density (Fig. 1f). In contrast, the intensity at (2, 0, 1.6) increased relatively sharply at around −0.4 V, the potential at which the change in the vertical expansion of the surface layer was observed (Fig. 1g). Both signals remained roughly constant at potentials below −0.4 V until close to the lower potential limit, where a small increase in the intensity was observed at (1, 1, 1.5) and a small decrease at (2, 0, 1.6). Although an unambiguous correlation of these signals with specific structural parameters is not possible, they confirm that the main changes in surface morphology occur in the potential range in which cluster formation was observed in the STM experiments and indicate that this transition occurs rather quickly.

Surface structural changes on the molecular scale

The formation of Cu nanoclusters leads to an irreversible modification of the surface structure on the molecular level. As shown previously,

freshly prepared Cu(100) electrodes are covered by a well-ordered adlayer with a complex long-range structure, which can be attributed to the co-adsorption of carbonate anions and water (Supplementary Fig. 6a,b)[33]. Starting from such an ordered carbonate adlayer with a $(\sqrt{2} \times 6\sqrt{2})R45°$ structure (Fig. 2a), the potential was decreased from 0.1 to −0.27 V, where Cu nanoclusters emerged on the surface (Fig. 2b). Close inspection of the Cu terraces surrounding these clusters revealed a highly disordered adlayer in which molecular species are clearly discernible, that is, they are sufficiently immobile to be imaged by STM, but vary strongly in their apparent height and intermolecular spacing. Changing the potential back to 0.1 V resulted in the disappearance of the clusters from the surface; however, the ordered carbonate adlayer structure did not reappear (Fig. 2c). Instead, an adlayer with only short-range order was observed. This disordered adlayer phase was rather stable, although some slow changes in the lateral arrangement of the species were observed on a timescale of minutes (Supplementary Fig. 7). Nevertheless, the ordered carbonate adlayer on the Cu surface could not be recovered even after applying a potential of -0.1 V for more than 1 h. This surface phase behaviour strongly differs from that observed in in situ STM experiments in which the potential was kept positive of the range of cluster formation. In these experiments, the ordered carbonate adlayer underwent a highly reversible surface phase transition to a disordered, mobile adlayer phase at 0 V, which reordered after increasing the potential again above 0 V (ref. 33). Thus, the irreversible modification of the molecular adlayer structure is directly linked to the formation of Cu clusters.

For insight into the origin of the irreversible changes, we analysed the structure of the disordered adlayer in more detail. Assigning the maxima in the STM images to individual adsorbate species, we obtained their characteristic lateral distances using the autocorrelation function, which yielded a distance of about 1.1 ± 0.1 nm between neighbouring adsorbates on the disordered adlayer at 0.1 V (Supplementary Fig. 6h). This is similar to the characteristic distances between the most pronounced maxima within the ordered $(\sqrt{2} \times 6\sqrt{2})R45°$ and (4×4) carbonate adlayer structures, although in those cases additional weaker maxima could be observed between the main maxima[33]. Furthermore, the vertical modulation of the disordered adlayer is much higher than that of the ordered carbonate adlayer phases. Cross-sections of the STM images show an average height variation of ~0.05 nm among the disordered maxima, whereas the variation in the initial $(\sqrt{2} \times 6\sqrt{2})R45°$ layer is only ~0.03 nm (Supplementary Fig. 6). In addition, isolated maxima with an even greater apparent height of up to 0.16 nm and small pits with depths of up to 0.13 nm were found on the surface of the disordered phase. All these observations indicate that Cu cluster formation induces an irreversible roughening of the surface on the molecular scale, in good agreement with the SXRD results.

We accordingly attribute the irreversible changes in the adlayer structure to the presence of Cu adatoms and surface vacancies that remain on the electrode after dissolution of the nanoclusters. The presence of such surface defects is supported by the CTR analysis and the persisting depressions observed in the nanoscale STM images after a potential excursion to values below −0.2 V. These defects are trapped in the carbonate adlayer formed above 0 V and disrupt the adlayer's structure, preventing its long-range ordering.

Potential-dependent composition of the adlayer on Cu

To identify the chemical nature of the adsorbate species on the Cu surface under the conditions used in the in situ STM and SXRD studies, we conducted complementary in situ SERS experiments on Cu(100) in CO_2-saturated 0.1 M $KHCO_3$ solution. The copper electrodes were pretreated by oxidation–reduction cycles (see Supplementary Fig. 12 and Methods for details), kept at 0.25 V until the Cu oxide was fully reduced and then studied during a stepwise cathodic potential cycle. The characteristic SERS bands in the Cu(100) spectra are displayed in Fig. 2d

(full spectra are given in Supplementary Fig. 13). The spectra show a potential-dependent behaviour. In the double layer range, the bands at 360 and 1,540 cm^{-1} and at 1,050 and 1,072 cm^{-1} are dominant. These have been assigned to bidentate carbonates ($*O_2CO$) and (bi)carbonate anions (HCO_3^- and CO_3^{2-}) on or near the surface, respectively[34–36]. Also, the weak band that emerges at ~1,000 cm^{-1} in the positive potential sweep has been attributed to either dissolved bicarbonate or adsorbate species related to formate or formic acid[37,38]. In some studies, the bands at 360 and 1,540 cm^{-1} have also been linked to the reduction of oxide species such as $CuCO_3$ (refs. 26,32). These bands disappear at potentials below −0.05 V, and at the same potential the (bi)carbonate bands also decrease significantly, so that at potentials around −0.51 V only peaks of very low intensity remain. However, the (bi)carbonate bands do not disappear completely, even at higher overpotentials, in line with the literature[26,32,34]. On scanning back to potentials up to 0.25 V, the carbonate band at 1,090 cm^{-1} maintains its low intensity and the band at 360 cm^{-1} only reappears with low intensity. This behaviour strongly resembles the irreversible changes in the molecular adlayer structure observed by STM. Specifically, the initial strong bands at 360, 1,070 and 1,540 cm^{-1} seem to be associated with carbonate bound to the initial defect-free Cu(100) terraces and are not restored in the back scan.

Parallel to the decrease in the bidentate carbonate bands at 360 and 1,540 cm^{-1}, new bands at 1,390 and 1,610 cm^{-1} emerge at −0.05 V that disappear again at potentials below −0.33 V. These bands stem from the symmetric and asymmetric vibrations of adsorbed carboxylate or carboxy groups, respectively, which can be attributed to the first reduction intermediates of CO_2 (ref. 39). In the reverse potential scan back to more positive values, these bands reappear at −0.33 V and then maintain a roughly constant intensity up to 0.25 V. Again, this resembles the irreversible behaviour observed in the STM studies and indicates that once these intermediates are formed, they remain on the Cu surface even at positive potentials.

In the negative potential regime, the carboxylate intermediate is reduced to adsorbed CO on the surface starting from −0.24 V. This is evidenced by the emergence of the characteristic Cu–CO rotation and stretching bands at 280 and 360 cm^{-1}, respectively, and the concomitant formation of broad bands in the range 1,900–2,100 cm^{-1}. These broad CO Raman peaks appear in the same potential range as the Cu nanocluster, indicating that the formation of the CO intermediate promotes this type of copper restructuring in the carbonate electrolyte, and are known to be stable at higher overpotentials of around −1.0 V[32,40]. Furthermore, a detailed analysis of the CO bands in the high and low Raman shift region (Supplementary Note 2 and Supplementary Figs. 14–16) indicates a reversible process in which a low coverage of bridge-bound CO at low overpotentials is converted at higher overpotentials into a CO_2RR-active atop configuration with a higher CO coverage. Only at −0.24 V CO_{atop} already shows a higher coverage than CO_{bridge} coverage in the cathodic scan. This might be related to the dominant bonding of CO to the Cu nanocluster at these low overpotentials.

Finally, a broad band at 2,900 cm^{-1} emerges at potentials below −0.04 V during the potential decrease, concomitant with carboxylate formation, and does not disappear during the subsequent potential sweep in the positive direction (Supplementary Fig. 13). This is in very good agreement with the SERS studies of Jian et al., who reported a similar Raman peak in this area and assigned it to a variety of species containing C–H bonds (for example, carboxylate, formate and ethylene) with different adsorption modes[26]. This observation again strongly indicates that some intermediates are formed irreversibly on the surface. Thus, the disordered layer observed in our STM experiments is composed of several molecular species.

Mechanisms of Cu surface restructuring under CO_2RR conditions

Our in situ STM, SXRD and SERS results demonstrate unambiguously a dynamic restructuring of planar Cu(100) electrodes in CO_2-saturated

carbonate solution. The observed formation of nanoscale clusters can be attributed to the formation of CO intermediates. A similar restructuring process was postulated previously by Gunathunge et al. based on in situ vibrational spectroscopy studies of CO on polycrystalline Cu electrodes, who assigned the high-frequency band to CO adsorbed on Cu clusters[25]. On the basis of that assignment, Cu restructuring was proposed to start at around −0.6 V and to be highly reversible. While our SERS data are in agreement with the results of Gunathunge et al., our STM studies show that cluster formation already occurs at potentials that are about 400 mV more positive than this. Thus, the high-frequency CO band is either related to another process, for example, the large-scale Cu restructuring reported by Kim and co-workers for polycrystalline Cu[15,16], or indicates a change in the CO adsorption geometry.

According to our results, Cu nanocluster formation commences at the very onset of CO formation. This seems reasonable taking into account that cluster formation was observed at CO partial pressures as low as 0.1 mbar in gas-phase studies[17,18,41]. The clusters form within less than 1 min and then reach a saturation density on the surface. For longer times at potentials below −0.2 V, both STM (Supplementary Figs. 2 and 5) and SXRD (Fig. 1f) measurements indicate that there is no major change in the surface density of the clusters. In particular, the total coverage of Cu atoms that are extracted from the surface layer and form clusters remains a small percentage of a monolayer, even after maintaining the Cu electrode in the negative potential regime for hours. This behaviour is surprising considering the substantial increase in CO surface coverage found by SERS in this potential range (Supplementary Figs. 15 and 16). Apparently, further adsorption of CO occurs on the planar Cu(100) terraces rather than inducing the formation of low-coordinated Cu adatoms and nanoclusters. This is also supported by the pronounced vertical expansion of the Cu surface layer spacing d_{12} observed below −0.3 V in the SXRD studies (Fig. 1g), which can be attributed to CO chemisorption on top of this surface layer.

To explain why the nanocluster density remains low, we first note that considerably more extensive restructuring was observed in a CO gas atmosphere[17,18]. Thus, the low density is not related to an intrinsic limitation of CO-induced restructuring of Cu surfaces. Furthermore, we recall that in KHCO₃ solution, Cu nanoclusters seem to be formed only in a narrow potential window, but then are stable on the surface even at much more negative potentials. This indicates that the low cluster density is due to kinetic limitations, most likely concerning Cu extraction from the surface via the formation of Cu adatom–vacancy pairs.

The limited Cu cluster formation in KHCO₃ solution can be attributed to the presence of molecular co-adsorbates and electric fields at the interface, both of which can affect CO-induced cluster formation. Relevant molecular adsorbate species are (bi)carbonate and carboxylates, which are co-adsorbed with CO in the potential range of −0.24 to −0.44 V and are gradually replaced by it. These species provide a chemical environment that is distinctly different from the case of pure CO and may influence the CO-induced formation of Cu adatoms and clusters. Specifically, the molecular co-adsorbates may bind to these low-coordinated Cu atoms as well as to the surrounding Cu substrate, which will affect the CO–Cu interactions. Our observation that carboxylates are found in the disordered adlayer phase up to potentials of 0.25 V provides support for a mutual stabilization of these species and Cu adatoms. The influence of electric fields on the free energy of adatom formation has been addressed in DFT calculations by Müller and Ibach[42]. For Cu atoms on Cu(100), a strong increase in the energy of formation with decreasing potential was found, which would qualitatively account for the termination of cluster formation at high overpotentials. Similar potential effects may be expected for CO-induced Cu adatom formation, but these have not been addressed in ab initio theory studies up to now.

On subsequently increasing the potential, the clusters become unstable above −0.2 V. However, the adatoms that formed the clusters remain on the Cu surface. Again, this can be explained by the molecular
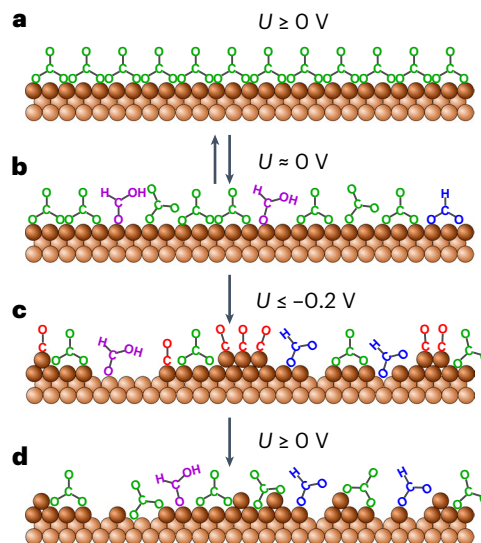
Fig. 3 | Schematic of the proposed mechanism for the formation of low-coordinated Cu species. a–**c**, Starting from a planar Cu surface with an ordered carbonate adlayer (**a**), decreasing the potential (*U*) leads to a reversible transition to a disordered (bi)carbonate/carboxylate adlayer (**b**), followed by CO-induced formation of Cu nanoclusters and vacancy islands (**c**). **d**, Increasing the potential back to the double layer regime, the Cu clusters disperse into isolated Cu adatoms, resulting in a disordered adlayer of mutually stabilizing carbonate/carboxylate adsorbates and Cu surface defects.

adlayer on the surface, which strongly hinders the surface mobility of the adatoms and the recombination of adatoms with vacancies. On decreasing the potential, the presence of Cu adatoms and vacancies will lead to local configurations that strongly bind the molecular species and thus prevent their reordering into the two-dimensional adlayer phases observed on atomically smooth Cu(100) above 0 V. Indeed, high-resolution STM images (Fig. 2c) indicate that the adlayer is a disordered assembly of different adsorbate species, Cu adatoms and vacancies and show a very low surface mobility in this phase.

In total, the results of our study indicate a microscopic scenario of molecular-scale structural changes on Cu electrodes in CO₂-saturated KHCO₃ solution, as illustrated in Fig. 3. In the double layer range, the Cu surface is covered by an ordered adlayer of carbonate and co-adsorbed water molecules (Fig. 3a), as described previously[33]. Decreasing the potential below 0 V results in adlayer disordering and the formation of the first reaction intermediates, such as carboxylates (Fig. 3b). This order–disorder transition in the adlayer is highly reversible at potentials above −0.2 V. Below −0.2 V, the carboxylate intermediates are reduced to adsorbed CO, which induces the extraction of Cu atoms out of the surface layer, leading to the formation of Cu adatoms and surface vacancies (Fig. 3c). These coalesce to form nanoscale adatom clusters and vacancy islands, similar to those found on Cu surfaces that are directly exposed to dissolved or gaseous CO. The Cu extraction process is limited to much lower cluster surface densities than is expected on the basis of the data for CO-induced cluster formation in the gas phase, which most probably is a result of the presence of other molecular co-adsorbates. At more negative potentials, the created adatoms and nanoclusters remain on the surface down to −1.1 V. On subsequently increasing the potential, the Cu nanoclusters decay above −0.2 V to form isolated Cu adatoms that remain on the surface (Fig. 3d). The recombination of Cu adatoms and vacancies is strongly kinetically hindered because the adatoms and CO₂RR reaction intermediates are mutually stabilizing each other, resulting in a highly disordered mixed adlayer of these species. It might be expected that the presence of such defects on the surface would assist the formation of Cu clusters if the potential were lowered again below −0.2 V, because

clusters can now form not only by the extraction of atoms from the Cu surface layer, but also by the re-aggregation of Cu adatoms that are already present on the surface and are highly mobile. This was indeed observed in an STM experiment in which a significantly higher cluster surface density was observed in a second potential cycle (Supplementary Fig. 8).

The irreversible formation of low-coordinated Cu surface atoms by these restructuring processes is expected to be of significant relevance for the CO$_2$RR, as such surface species may provide preferred binding sites for CO$_2$RR intermediates. Consequently, their presence on the surface should affect the CO$_2$RR activity and selectivity of the Cu surface. This is supported by recent ab initio calculations by Lopez and co-workers[43,44]. Here, it was found that four- and six-fold coordinated copper adatoms can tether CO$_2$ more strongly than planar single-crystal Cu surfaces and thus activate it for the CO$_2$RR. Furthermore, DFT studies by Bagger et al.[45] and previous experimental work by our group and others found that undercoordinated sites are favourable for the formation of ethylene and other hydrocarbons, while highly disordered surfaces encompassing metallic and cationic Cu species favour oxygenates such as ethanol[7,8,23]. As the observed restructuring is a highly local process that occurs on length scales on the order of 1 nm, it is also expected to occur at the facets of more complex CO$_2$RR electrocatalysts, such as polycrystalline Cu and Cu catalyst particles. Indeed, studies of such systems also indicated Cu restructuring during the CO$_2$RR, which was explained by atomic-scale processes on the surface[27,28,46–49]. Here, we have presented mechanistic insights into these atomic-scale processes.

Conclusions

The in situ STM, SXRD and SERS data collected in this study indicate that the onset of CO formation in bicarbonate solution induces the formation of Cu nanoclusters on the surface of Cu electrodes. This process is kinetically limited, proceeds in a narrow potential range and leads to the spontaneous irreversible formation of low-coordinated Cu species on the electrode surface. The latter process corresponds to an additional Cu surface restructuring mechanism on the near-atomic scale that complements the long-range structural transformations of the morphology of Cu surfaces reported in previous studies using alternative in situ methods[22]. The Cu surface restructuring reported here occurs at potentials at which the reduction current is very low and usually deemed to be technologically irrelevant. Nevertheless, it may still significantly affect the CO$_2$RR reactivity in the potential regime relevant for the formation of multi-carbon products as it creates Cu adatoms and nanoclusters, resulting in the formation of undercoordinated Cu atoms on atomically smooth terraces. According to the SXRD results, these undercoordinated Cu atoms are present on the surface over the entire potential range of the CO$_2$RR and their presence thus has to be taken into account in mechanistic studies of this reaction. Specifically, they provide low-coordinated sites that may be relevant and unavoidable for specific CO$_2$RR reaction pathways, resulting in the self-activation of the catalyst. Furthermore, our data indicate that the formation of clusters and their surface density are governed by kinetic effects. Thus, pulses into the potential range of cluster formation or related protocols may further increase or regenerate the cluster density. This might allow Cu electrodes to be activated under potentiodynamic conditions that are restricted to the CO$_2$RR regime, which may contribute to a better understanding of the active sites as well as providing a route to activating the Cu cathode without intermediate anodic polarization.

Methods

Sample preparation

All experiments were performed in 0.1 M KHCO$_3$ (Sigma-Aldrich), pretreated with Chelex 100 resin (Bio-Rad) to purify the electrolyte of trace metal ion impurities[50,51]. Before use, the as-received Chelex resin

was pretreated by stirring in 1 M HCl for 12 h and subsequent rinsing with 5 l ultrapure water (18.2 MΩ). In the next step, the Chelex resin was stirred in 1 M KOH for 24 h at about 70 °C and then rinsed with 8 l ultrapure water.

STM and SXRD experiments were performed on Cu(100) single crystals (MaTecK) prepared via at least three electropolishing cycles in 65–70% orthophosphoric acid (Merck) at potentials between 1.8 and 2.8 V versus a Pt wire counter electrode. In each electropolishing cycle, the sample was electropolished for ~10 s and then rinsed with ultrapure water. After the last cycle, the copper electrode was protected with a droplet of water or 0.1 M H$_2$SO$_4$, prepared from ultrapure sulfuric acid (Merck), and mounted in the electrochemical STM or SXRD cell, respectively.

For the SERS measurements, roughened Cu(100) served as the working electrode to achieve sufficient surface-enhancement of the Raman signal. The electrodes were prepared by electropolishing in concentrated H$_3$PO$_4$ (85% for analysis, PanReac Applichem) against a titanium mesh. The Cu(100) sample was first electropolished for 3 min at 2.8 V, followed by three cycles at 3 V (each cycle ≈ 10 s). After each cycle, the electrode was rinsed with ultrapure water.

STM imaging

All STM experiments were performed in an electrochemical environment using a PicoPlus 5500 scanning probe microscope (Agilent) in constant current mode. Two platinum wires were used as the counter and pseudo-reference electrodes. The pseudo-reference electrode was calibrated by measurements versus a standard calomel electrode and cyclic voltammetry after the experiments. It should be noted that the immersion of Cu(100) in KHCO$_3$ solution at the open circuit potential leads to pronounced roughening of the surface. To avoid this, the Cu(100) sample was first immersed in 0.1 M H$_2$SO$_4$, a potential in the range of 0.05 to 0.15 V was applied and finally the electrolyte was exchanged under potential control to 0.1 M KHCO$_3$.

The electrolyte volume within the electrochemical cell was about 100 μl and the thickness of the electrolyte above the Cu(100) electrode was about 1–2 mm. The electrochemical cell was kept under CO$_2$ atmosphere throughout the STM experiments, which were performed using tunnelling currents of 0.05 to 0.7 nA and bias voltages of −0.09 to −0.7 V. The data were analysed using the SPIP (https://www.imagemet.com/) and Gwyddion[52] software as well as Python scripts. High-pass filtering was applied to some of the images to increase the contrast of the Cu terraces.

SXRD experiments

The in situ SXRD measurements were carried out at the P23 beamline of the PETRA III synchrotron at Deutsches Elektronen-Synchrotron (DESY) using an X-ray energy of 22.5 keV. For all datasets, a constant angle of incidence of 2° was used. Hat-shape Cu(100) crystals with an orientation accuracy of ±0.1° (MaTecK) were used. The crystals were mounted in a home-built electrochemical flow cell[53] made from PEEK and containing a Pt wire counter electrode and an Ag/AgCl reference electrode (eDAQ ET072-1) in the electrolyte outlet and inlet, respectively. Potentials were applied and the corresponding currents were recorded using a Biologic SP-300 potentiostat. The CO$_2$-saturated 0.1 M KHCO$_3$ electrolyte was continuously exchanged using syringe pumps (Hamilton) at a rate of 5 μl s^{-1} to minimize radiolysis by the X-ray beam and the effects of bubble formation. However, the latter could not be eliminated completely and fluctuations in X-ray intensity of up to 15% were observed during the measurements, which we attribute to the release of bubbles. CTRs were collected in the double layer region at 0.0, −0.1, −0.2 and −0.3 V, and in the CO$_2$RR region at −0.4, −0.7 and −1.1 V. The (11l), (20l), (22l) and (31l) CTRs were acquired at each potential. The CTR data were quantitatively fitted using the SuPeRod program within the DaFy software package[54]. This model refinement program uses the differential evolution algorithm fitting

engine derived from GenX; the errors were estimated by varying each model parameter until a 5% variation of the optimal figure of merit was achieved[55].

Raman measurements

In situ SERS experiments were conducted with a Raman spectrometer (Renishaw, InVia Reflex) coupled to an optical microscope (Leica Microsystems, DM2500M) and a motorized stage (Renishaw, MS300 encoded stage). The system was calibrated using a Si(100) wafer (520.5 cm^{-1}). A HeNe laser (Renishaw, RL633, wavelength = 633 nm, maximum power = 17 mW, grating = 1,800 lines mm^{-1}) served as the excitation source. The laser was focused on the top of the sample surface and Raman scattering signals were collected with a water immersion objective (Leica microsystems, ×63, numerical aperture = 0.9), which was protected from the electrolyte by a Teflon film (fluorinated ethylene propylene, GoodFellow, film thickness = 0.0125 mm). The electrochemical SERS measurements were conducted in a home-built spectroelectrochemical single-compartment cell and controlled using a Biologic SP240 potentiostat[32]. The cell was equipped with a leak-free Ag/AgCl reference electrode (LF-1-63, 1 mm diameter, Innovative Instruments) positioned close to the sample and a Pt counter electrode at the side of the cell (volume = 15 ml, electrolyte thickness above the working electrode ≈ 2.2 mm). The electrolyte (0.1 M $KHCO_3$) was constantly purged with CO_2 inside the cell. Freshly polished Cu(100) working electrodes were roughened by three cyclic voltammetric scans at 10 mV s^{-1}. The potential was swept from +0.25 V to +1.69 V and then back to +0.25 V in CO_2-saturated 0.1 M $KHCO_3$ inside the electrochemical SERS cell. This procedure resulted in a SERS-active Cu sample that was free of Cu_2O (Supplementary Figs. 12 and 13) and thus suitable for comparison with the STM and SXRD results. Afterwards, the potential was decreased stepwise to −0.58 V and then increased back to +0.25 V. SERS spectra were recorded at each potential until a steady state was reached (typically 5–10 min). The Raman spectra were collected in the extended mode and the scans were repeated at least once. The collection time for each spectrum was 10 s. The Raman data were then first processed using the Renishaw WiRE 5.2 software (https://www.renishaw.com/en/raman-software--9450) to normalize the spectra to a mean intensity of 0 and variance of 1 (if not stated otherwise) and to remove cosmic rays. We used Octave scripts to fit the Raman bands corresponding to CO[56].

Data availability

All data that support the findings of this study are available within the article and the Supplementary Information, or from the corresponding author upon reasonable request.

Code availability

The customized software package used for structure factor determination from SXRD data and the CTR data fitting is available at https://github.com/jackey-qiu/DaFy.

References

1. Hori, Y. In *Modern Aspects of Electrochemistry* **42**, 89–189 (MAOE, 2008).
2. Nitopi, S. et al. Progress and perspectives of electrochemical CO_2 reduction on copper in aqueous electrolyte. *Chem. Rev.* **119**, 7610–7672 (2019).
3. Birdja, Y. Y. et al. Advances and challenges in understanding the electrocatalytic conversion of carbon dioxide to fuels. *Nat. Energy* **4**, 732–745 (2019).
4. Hori, Y., Takahashi, I., Koga, O. & Hoshi, N. Selective formation of C_2 compounds from electrochemical reduction of CO_2 at a series of copper single crystal electrodes. *J. Phys. Chem. B* **106**, 15–17 (2002).
5. Roberts, F. S., Kuhl, K. P. & Nilsson, A. High selectivity for ethylene from carbon dioxide reduction over copper nanocube electrocatalysts. *Angew. Chem.* **127**, 5268–5271 (2015).
6. Huang, Y., Handoko, A. D., Hirunsit, P. & Yeo, B. S. Electrochemical reduction of CO_2 using copper single-crystal surfaces: effects of CO* coverage on the selective formation of ethylene. *ACS Catal.* **7**, 1749–1756 (2017).
7. Arán-Ais, R. M., Scholten, F., Kunze, S., Rizo, R. & Roldan Cuenya, B. The role of in situ generated morphological motifs and Cu(I) species in C_{2+} product selectivity during CO_2 pulsed electroreduction. *Nat. Energy* **5**, 317–325 (2020).
8. Timoshenko, J. et al. Steering the structure and selectivity of CO_2 electroreduction catalysts by potential pulses. *Nat. Catal.* **5**, 259–267 (2022).
9. Jeon, H. S. et al. Selectivity control of Cu nanocrystals in a gas-fed flow cell through CO_2 pulsed electroreduction. *J. Am. Chem. Soc.* **143**, 7578–7587 (2021).
10. Auer, A. & Kunze-Liebhäuser, J. In *Reference Module in Chemistry, Molecular Sciences and Chemical Engineering* (Elsevier, 2023).
11. Matsushima, H., Taranovskyy, A., Haak, C., Gründer, Y. & Magnussen, O. M. Reconstruction of Cu(100) electrode surfaces during hydrogen volution. *J. Am. Chem. Soc.* **131**, 10362–10363 (2009).
12. Huynh, T. M. T. & Broekmann, P. From in situ towards in operando conditions: scanning tunneling microscopy study of hydrogen intercalation in Cu(111) during hydrogen evolution. *ChemElectroChem* **1**, 1271–1274 (2014).
13. Zhang, Z., Wei, Z., Sautet, P. & Alexandrova, A. N. Hydrogen-induced restructuring of a Cu(100) electrode in electroreduction conditions. *J. Am. Chem. Soc.* **144**, 19284–19293 (2022).
14. Auer, A., Ding, X., Bandarenka, A. S. & Kunze-Liebhäuser, J. The potential of zero charge and the electrochemical interface structure of Cu(111) in alkaline solutions. *J. Phys. Chem. C* **125**, 5020–5028 (2021).
15. Kim, Y.-G., Baricuatro, J. H. & Soriaga, M. P. Surface reconstruction of polycrystalline Cu electrodes in aqueous $KHCO_3$ electrolyte at potentials in the early stages of CO_2 reduction. *Electrocatalysis* **9**, 526–530 (2018).
16. Kim, Y.-G., Baricuatro, J. H., Javier, A., Gregoire, J. M. & Soriaga, M. P. The evolution of the polycrystalline copper surface, first to Cu(111) and then to Cu(100), at a fixed CO_2RR potential: a study by operando EC-STM. *Langmuir* **30**, 15053–15056 (2014).
17. Eren, B. et al. Activation of Cu(111) surface by decomposition into nanoclusters driven by CO adsorption. *Science* **351**, 475–478 (2016).
18. Eren, B. et al. One-dimensional nanoclustering of the Cu(100) surface under CO gas in the mbar pressure range. *Surf. Sci.* **651**, 210–214 (2016).
19. Auer, A. et al. Self-activation of copper electrodes during CO electro-oxidation in alkaline electrolyte. *Nat. Catal.* **3**, 797–803 (2020).
20. Lee, S. H. et al. Oxidation state and surface reconstruction of Cu under CO_2 reduction conditions from in situ X-ray characterization. *J. Am. Chem. Soc.* **143**, 588–592 (2020).
21. Phan, T. H. et al. Emergence of potential-controlled Cu-nanocuboids and graphene-covered Cu-nanocuboids under operando CO_2 electroreduction. *Nano Lett.* **21**, 2059–2065 (2021).
22. Simon, G. H., Kley, C. S. & Roldan Cuenya, B. Potential-dependent morphology of copper catalysts during CO_2 electroreduction revealed by in situ atomic force microscopy. *Angew. Chem. Int. Ed.* **60**, 2561–2568 (2021).
23. Scholten, F., Nguyen, K.-L. C., Bruce, J. P., Heyde, M. & Roldan Cuenya, B. Identifying structure–selectivity correlations in the electrochemical reduction of CO_2: a comparison of well-ordered atomically clean and chemically etched copper single-crystal surfaces. *Angew. Chem. Int. Ed.* **60**, 19169–19175 (2021).
24. Wuttig, A. et al. Tracking a common surface-bound intermediate during CO_2-to-fuels catalysis. *ACS Cent. Sci.* **2**, 522–528 (2016).

25. Gunathunge, C. M. et al. Spectroscopic observation of reversible surface reconstruction of copper electrodes under CO_2 reduction. *J. Phys. Chem. C* **121**, 12337–12344 (2017).

26. Jiang, S., Klingan, K., Pasquini, C. & Dau, H. New aspects of operando Raman spectroscopy applied to electrochemical CO_2 reduction on Cu foams. *J. Chem. Phys.* **150**, 041718 (2019).

27. Huang, J. et al. Potential-induced nanoclustering of metallic catalysts during electrochemical CO_2 reduction. *Nat. Commun.* **9**, 3117 (2018).

28. Osowiecki, W. T. et al. Factors and dynamics of Cu nanocrystal reconstruction under CO_2 reduction. *ACS Appl. Energy Mater.* **2**, 7744–7749 (2019).

29. Bagger, A., Arnarson, L., Hansen, M. H., Spohr, E. & Rossmeisl, J. Electrochemical CO reduction: a property of the electrochemical interface. *J. Am. Chem. Soc.* **141**, 1506–1514 (2019).

30. Bagger, A. et al. Ab initio cyclic voltammetry on Cu(111), Cu(100) and Cu(110) in acidic, neutral and alkaline solutions. *ChemPhysChem* **20**, 3096–3105 (2019).

31. Dietterle, M., Will, T. & Kolb, D. The initial stages of copper deposition on Ag(111): an STM study. *Surf. Sci.* **342**, 29–37 (1995).

32. Zhan, C. et al. Revealing the CO coverage-driven C–C coupling mechanism for electrochemical CO_2 reduction on Cu_2O nanocubes via operando Raman spectroscopy. *ACS Catal.* **11**, 7694–7701 (2021).

33. Amirbeigiarab, R., Bagger, A., Tian, J., Rossmeisl, J. & Magnussen, O. M. Structure of the (bi)carbonate adlayer on Cu(100) electrodes. *Angew. Chem. Int. Ed.* **61**, 202211360 (2022).

34. De Ruiter, J. et al. Probing the dynamics of low-overpotential CO_2-to-CO activation on copper electrodes with time-resolved Raman spectroscopy. *J. Am. Chem. Soc.* **144**, 15047–15058 (2022).

35. Moradzaman, M. & Mul, G. In situ Raman study of potential-dependent surface adsorbed carbonate, CO, OH, and C species on Cu electrodes during electrochemical reduction of CO_2. *ChemElectroChem* **8**, 1478–1485 (2021).

36. Rüscher, M. et al. Tracking heterogeneous structural motifs and the redox behaviour of copper–zinc nanocatalysts for the electrocatalytic CO_2 reduction using operando time resolved spectroscopy and machine learning. *Catal. Sci. Technol.* **12**, 3028–3043 (2022).

37. Klingan, K. et al. Reactivity determinants in electrodeposited Cu foams for electrochemical CO_2 reduction. *ChemSusChem* **11**, 3449–3459 (2018).

38. He, M. et al. Selective enhancement of methane formation in electrochemical CO_2 reduction enabled by a Raman-inactive oxygen-containing species on Cu. *ACS Catal.* **12**, 6036–6046 (2022).

39. Shan, W. et al. In situ surface-enhanced Raman spectroscopic evidence on the origin of selectivity in CO_2 electrocatalytic reduction. *ACS Nano* **14**, 11363–11372 (2020).

40. Herzog, A. et al. Operando investigation of Ag-decorated Cu_2O nanocube catalysts with enhanced CO_2 electroreduction toward liquid products. *Angew. Chem. Int. Ed.* **60**, 7426–7435 (2021).

41. Roiaz, M. et al. Roughening of copper (100) at elevated CO pressure: Cu adatom and cluster formation enable CO dissociation. *J. Phys. Chem. C* **123**, 8112–8121 (2018).

42. Müller, J. & Ibach, H. Migration of point defects at charged Cu, Ag, and Au (100) surfaces. *Phys. Rev. B* **74**, 085408 (2006).

43. Dattila, F., García-Muelas, R. & López, N. Active and selective ensembles in oxide-derived copper catalysts for CO_2 reduction. *ACS Energy Lett.* **5**, 3176–3184 (2020).

44. Dattila, F., Seemakurthi, R. R., Zhou, Y. & López, N. Modeling operando electrochemical CO_2 reduction. *Chem. Rev.* **122**, 11085–11130 (2022).

45. Bagger, A., Ju, W., Varela, A. S., Strasser, P. & Rossmeisl, J. Electrochemical CO_2 reduction: classifying Cu facets. *ACS Catal.* **9**, 7894–7899 (2019).

46. Kim, D., Kley, C. S., Li, Y. & Yang, P. Copper nanoparticle ensembles for selective electroreduction of CO_2 to C_2–C_3 products. *Proc. Natl Acad. Sci. USA* **114**, 10560–10565 (2017).

47. Yang, Y. et al. Operando studies reveal active Cu nanograins for CO_2 electroreduction. *Nature* **614**, 262–269 (2023).

48. Vavra, J., Shen, T.-H., Stoian, D., Tileli, V. & Buonsanti, R. Real-time monitoring reveals dissolution/redeposition mechanism in copper nanocatalysts during the initial stages of the CO_2 reduction reaction. *Angew. Chem.* **133**, 1367–1374 (2021).

49. Li, Y. et al. Electrochemically scrambled nanocrystals are catalytically active for CO_2-to-multicarbons. *Proc. Natl Acad. Sci. USA* **117**, 9194–9201 (2020).

50. Wuttig, A. & Surendranath, Y. Impurity ion complexation enhances carbon dioxide reduction catalysis. *ACS Catal.* **5**, 4479–4484 (2015).

51. Gao, D. et al. Activity and selectivity control in CO_2 electroreduction to multicarbon products over CuO_x catalysts via electrolyte design. *ACS Catal.* **8**, 10012–10020 (2018).

52. Nečas, D. & Klapetek, P. Gwyddion: an open-source software for SPM data analysis. *Cent. Eur. J. Phys.* **10**, 181–188 (2012).

53. Reikowski, F. et al. Operando surface X-ray diffraction studies of structurally defined Co_3O_4 and CoOOH thin films during oxygen evolution. *ACS Catal.* **9**, 3811–3821 (2019).

54. Qiu, C. Data Analysis Factory (DaFy); https://github.com/jackey-qiu/DaFy/wiki

55. Björck, M. & Andersson, G. GenX: an extensible X-ray reflectivity refinement program utilizing differential evolution. *J. Appl. Cryst.* **40**, 1174–1178 (2007).

56. Eaton, J. W., Bateman, D., Hauberg, S. & Wehbring, R. (2019). GNU Octave version 4.0. 0 manual: a high-level interactive language for numerical computations. 2015. http://www.gnu.org/software/octave/doc/interpreter, 8, 13.

Author contributions

O.M.M., R.A., J.T., A.H. and A.B. wrote the original paper. R.A. performed the STM measurements, including the data analysis. J.T., R.A., A.H., A.B., C.Q. and O.M.M. designed and performed the in situ SXRD experiments at DESY. J.T. analysed the SXRD data. A.H. performed the SERS measurements, including the data analysis. O.M.M. conceived the study and was responsible for project administration. All authors contributed to the discussion and interpretation of the data and revised the manuscript.

Competing interests

The authors declare no competing interests.

Additional information

Supplementary information The online version contains supplementary material available at https://doi.org/10.1038/s41929-023-01009-z.

Correspondence and requests for materials should be addressed to Olaf M. Magnussen.